Sensors and Materials, Vol. 38, No. 8 (2026) 4563–4576
MYU Tokyo

S & M 4582

Si_3N_4/Cr-based Ultra-broadband Optical Absorber Covering the UV–visible–mid-IR Range (300–3850 nm)

Jian Guo,[1] Chiawen Lee,[1*] Yu-Chen Tsai,[2] and Cheng-Fu Yang[2,3**]

[1]School of Information Engineering, Xiamen Ocean Vocational College, Xiamen 361102, China
[2]Department of Chemical and Materials Engineering, National University of Kaohsiung, Kaohsiung 811, Taiwan
[3]Department of Aeronautical Engineering, Chaoyang University of Technology, Taichung 413, Taiwan

(Received January 29, 2026; accepted August 5, 2026)

Keywords: Si_3N_4/Cr, ultra-broadband, optical absorber, UV–visible–mid-IR range, optical sensor

Ultra-broadband optical absorbers are essential components in modern photonic and sensing systems, where efficient light absorption over a wide spectral range is required to enhance device performance and environmental adaptability. In this study, a simple yet highly efficient ultra-broadband optical absorber is proposed using only two materials: silicon nitride (Si_3N_4) and chromium (Cr). The absorber features a nine-layer architecture, in which a Cr reflective layer forms the bottom substrate, followed by alternating planar Cr and Si_3N_4 layers from the second to the eighth layer. The topmost layer consists of Cr cylindrical structures that further enhance broadband absorption through additional optical coupling and intrinsic material loss. By systematically optimizing key structural parameters, including layer thicknesses and cylinder diameters, the proposed design achieves absorptivity exceeding 0.900 over an ultra-broadband wavelength range from 300 to 3850 nm. Compared with previously reported ultra-broadband absorbers that rely on complex nanostructures and multiple-material systems, the present design significantly simplifies fabrication and reduces the risk of vacuum process contamination while maintaining excellent optical performance. These results demonstrate a practical and scalable approach for realizing high-performance ultra-broadband optical absorbers, offering strong potential for applications in optical sensing, photodetection, and energy-related devices.

1. Introduction

Ultra-broadband optical absorbers have attracted significant attention in recent years owing to their ability to efficiently capture electromagnetic radiation over an exceptionally wide spectral range. In the design of an absorber, the term ultra-broadband is defined as a continuous wavelength region in which the absorptivity remains higher than 0.900. This criterion is widely adopted in the optical absorber literature because absorptivity above 90% is generally regarded as sufficient to suppress optical reflection and ensure efficient electromagnetic energy harvesting over a broad spectral range. Unlike narrowband or multiband absorbers, ultra-broadband absorbers are capable of suppressing reflection and transmission across ultraviolet

*Corresponding author: e-mail: lijiawen@xmoc.edu.cn
**Corresponding author: e-mail: cfyang@nuk.edu.tw
https://doi.org/10.18494/SAM6235

ISSN 0914-4935

(UV), visible, NIR, and even mid-IR (MIR) wavelengths, enabling comprehensive light–matter interaction. This capability is crucial for applications requiring high optical efficiency under broadband illumination conditions, such as energy harvesting, thermal emission control, photodetection, and optical shielding. From a physical perspective, achieving ultra-broadband absorption typically involves synergistic effects such as impedance matching, multiresonance coupling, intrinsic material loss, and enhanced optical path length through multiple reflections.

Ultra-broadband optical absorbers play a pivotal role in a wide range of sensing applications, where stable and efficient light absorption over broad spectral regions is essential for accurate signal detection and environmental adaptability. In optical and optoelectronic sensors, broadband absorbers facilitate efficient light harvesting over a wide spectral range and contribute to stable optical responses under different illumination conditions, making them attractive for various sensing applications.[1] Similarly, thermal sensors,[2] IR imagers,[3] and bolometers[4] rely on broadband absorbers to convert incident radiation into heat with high efficiency, directly impacting device sensitivity and response time. In chemical and biological sensing, efficient optical interaction over broad spectral regions is beneficial for multispecies analysis and complex environmental monitoring, where optical sensing techniques continue to play an increasingly important role.[5,6] As sensor technologies increasingly move toward compact, multifunctional, and integrated systems, ultra-broadband optical absorbers have become indispensable components that underpin high-performance sensing across diverse operational environments.

Despite the substantial progress achieved in ultra-broadband absorber design, many previously reported structures rely on three or more constituent materials together with complex nanostructured geometries, such as multilayer gratings, metasurfaces, nanocone arrays, and hybrid metal–dielectric architectures, to achieve broadband absorption.[7–9] While such designs can achieve excellent absorption performance, they often introduce significant fabrication challenges. In most cases, each functional layer consists of nanoscale patterns that require high-resolution lithography and precise alignment, substantially increasing fabrication complexity and cost. Furthermore, the deposition of multiple dissimilar materials typically necessitates the repeated use of vacuum-based processes such as sputtering, evaporation, or atomic layer deposition. This multimaterial approach increases the risk of cross-contamination within vacuum systems, potentially degrading material purity, interface quality, and device reproducibility. In addition, frequent material switching prolongs processing time and complicates large-scale manufacturing. These factors collectively limit the practical applicability and scalability of many high-performance ultra-broadband absorbers. As a result, there is a growing need for absorber designs that reduce material diversity and structural complexity while maintaining or improving broadband absorption performance, thereby enabling more reliable fabrication and broader industrial adoption.

Multilayer planar architectures have emerged as an effective and practical strategy for realizing ultra-broadband optical absorption while avoiding the complexities associated with intricate nanostructures.[10,11] By stacking alternating lossy metallic layers and dielectric films, broadband absorption can be achieved by combining mechanisms such as Fabry–Pérot resonance, destructive interference, and gradual impedance matching across a wide spectral range. Compared with nanostructured metamaterial absorbers, planar multilayer designs offer

several notable advantages. First, they are inherently compatible with standard thin-film deposition techniques, enabling high uniformity and reproducibility over large areas. Second, planar structures significantly relax fabrication tolerances, as their optical response is primarily governed by layer thickness rather than nanoscale pattern fidelity. Third, the reduced reliance on lithography lowers fabrication cost and enhances scalability for industrial applications. Moreover, planar multilayer absorbers exhibit strong mechanical stability and environmental robustness, which are essential for long-term operation in sensing and energy-related devices. Recently, Hsu *et al.* reported a Cr–SiO_2 multilayer planar absorber employing alternating Cr and SiO_2 films with a top Cr cylindrical resonator.[12] Using a layer-by-layer optimization strategy similar to that adopted in our work, their design achieved an absorptivity exceeding 0.900 over the wavelength range of 200–2160 nm. These results demonstrate that simplified two-material multilayer architectures can provide excellent broadband absorption while maintaining fabrication compatibility. Nevertheless, the high-absorption region remained mainly within the UV–NIR range.

Motivated by the aforementioned advantages, we propose and demonstrate an ultra-broadband optical absorber based solely on two materials: silicon nitride (Si_3N_4) and chromium (Cr). One key innovation of this work is the use of Si_3N_4 as a primary dielectric material for ultra-broadband absorber design, which has rarely been explored in such applications. In addition, the proposed absorber achieves ultra-broadband performance using only a simplified two-material system composed of Si_3N_4 and Cr. The proposed absorber features a nine-layer architecture, in which the bottom Cr layer functions as a reflective substrate, while the second through eighth layers consist of alternating planar Cr and Si_3N_4 films. The topmost ninth layer is composed of Cr cylindrical structures that further enhance broadband absorption by introducing additional optical coupling and loss mechanisms. By limiting the material system to only Si_3N_4 and Cr, the proposed design significantly simplifies fabrication and minimizes the risk of vacuum system contamination. Because the proposed design preserves the same planar multilayer configuration as the previously reported Cr–SiO_2 absorber, replacing SiO_2 with Si_3N_4 does not introduce additional fabrication complexity or tighter dimensional tolerances. Therefore, the improved optical performance is achieved primarily through material substitution rather than structural modification, maintaining compatibility with conventional thin-film deposition processes. The geometric parameters of each layer, including thickness and cylinder diameter, are systematically optimized to achieve maximum absorption performance. As a result, the optimized absorber exhibits absorptivity exceeding 0.900 over an ultra-broadband wavelength range from 300 to 3850 nm. These results demonstrate that high-performance ultra-broadband absorption can be achieved using a simplified material system and a predominantly planar multilayer architecture, offering a promising route toward practical and scalable optical absorber designs.

2. Methodology

In this work, the optical absorption performance and effective impedance characteristics were evaluated through full-wave numerical simulations conducted using COMSOL

Multiphysics® (version 6.0). An ultra-broadband solar absorber based on a metamaterial architecture and composed exclusively of two cost-effective materials, Si_3N_4 and Cr, was designed. The unit-cell geometry of the proposed multilayer absorber, with a periodicity of 300 nm, is illustrated in Fig. 1 and consists of an eleven-layer configuration optimized for efficient electromagnetic energy dissipation. All optical parameters of Cr and Si_3N_4, including complex refractive indices, absorption coefficients, wavelength-dependent dispersion functions $n(\lambda)$ and $k(\lambda)$, and dielectric constants, were adopted directly from the built-in COMSOL material database to ensure realistic modeling. The geometric configuration and initial layer thicknesses were selected referring to the Cr–SiO_2 absorber reported in Ref. 13, and the same COMSOL simulation settings and material database were employed throughout this study. Therefore, the subsequent comparison between the Cr–SiO_2 reference design and the proposed Si_3N_4/Cr structure was carried out under a consistent numerical framework, allowing the effect of dielectric material substitution to be evaluated directly.[13]

The absorber structure incorporates a 100-nm-thick Cr layer (h1) as a bottom reflective substrate, followed by alternating planar layers of Si_3N_4 and Cr with precisely tailored thicknesses. Specifically, the Si_3N_4 layers (h2, h4, h6, and h8) were set to 85, 85, 85, and 20 nm, respectively, while the intermediate Cr layers (h3, h5, and h7) each had a thickness of 6 nm. The topmost Cr layer (h9) with a diameter (D) of 165 nm was increased to 100 nm to enhance broadband absorption. Subsequently, the parameters of each layer were systematically optimized through numerical simulations to design an ultra-broadband absorber exhibiting absorptivity higher than 0.900 across the UV to MIR spectral range. The numerical model employed a finely resolved tetrahedral mesh comprising 10688 nodes and 58237 volume elements, with grid sizes ranging from 0.83 to 1.65 nm. The mesh quality, characterized by an average element quality of 0.6339, ensured numerical stability and accuracy, providing a reliable foundation for the subsequent optical analysis. Periodic boundary conditions were applied to the lateral boundaries

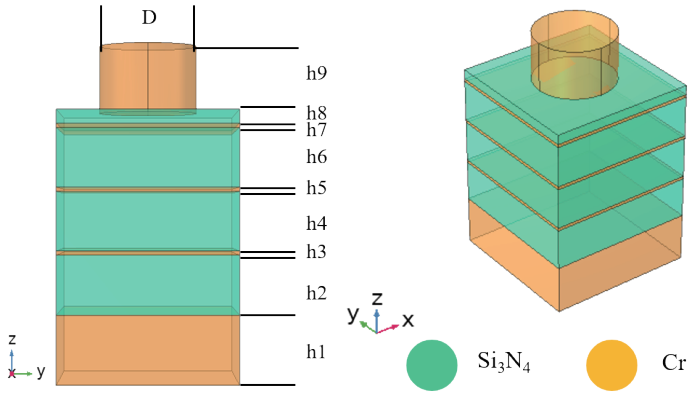

Fig. 1. (Color online) Structure of the investigated absorber. For clarity, the thicknesses shown in the schematic are not drawn to scale. The initial thicknesses of the intermediate Cr layers (h3, h5, and h7) are all 6 nm, as summarized in Table 2.

of the unit cell to model an infinitely periodic absorber array, while perfectly matched layers (PMLs) were employed along the propagation direction to suppress artificial reflections from the computational domain. A normally incident transverse electric (TE)-polarized plane wave was introduced from the air region above the absorber. Because the bottom Cr layer was designed with a thickness of 100 nm, which is considerably larger than the optical penetration depth of Cr, optical transmission through the structure is negligible over the investigated wavelength range. Therefore, the absorptivity was calculated as $A = 1 - R$, where R denotes the reflected power, and the normalized optical impedance was evaluated from the corresponding reflection coefficient.

3. Results and Discussion

First, the effect of the h1 Cr layer thickness on the absorption spectra was examined. When the thickness of the h1 Cr layer was varied from 80 to 120 nm with a step size of 10 nm, the overall absorption spectra exhibited nearly no observable change (not shown here). This behavior is primarily attributed to the fact that the h1 layer is located at the bottom of the absorber and functions as a bottom reflective substrate. Since the majority of optical absorption occurs within the upper layers (h2–h6), variations in the thickness of the h1 layer have a negligible impact on the overall absorption performance. Note that a small residual field can still be observed within the upper portion of the bottom Cr layer because electromagnetic waves penetrate a finite distance into lossy metals. This field corresponds to evanescent penetration rather than propagating transmission and decays rapidly with depth. Therefore, the 100 nm Cr layer still functions as an effective optical reflector that suppresses transmission while maintaining nearly complete optical confinement within the absorber.

Next, thickness optimization was performed for the h2 layer by parametric sweep in the range of 65 to 135 nm with a step size of 10 nm. As shown in Fig. 2(a), the absorptivity of the

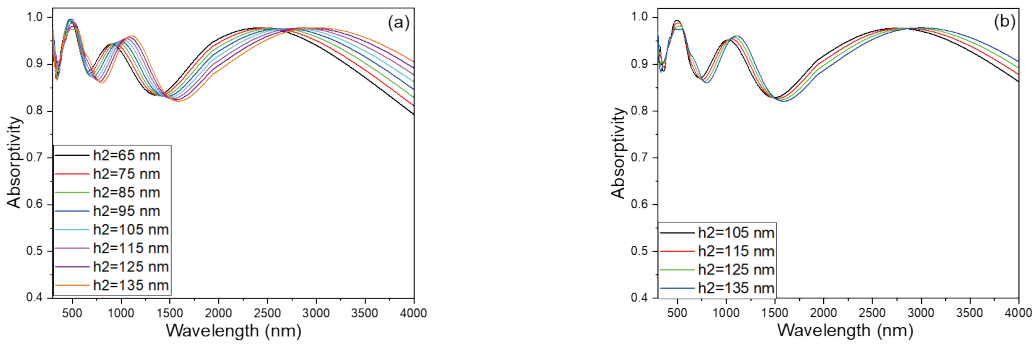

Fig. 2. (Color online) Effects of different thicknesses of h2 Si_3N_4 layer on absorption spectra, spanned from (a) 65–135 nm and (b) 105–135 nm.

Si_3N_4 layer (h2) beyond a wavelength of 3000 nm increases monotonically with thickness. This behavior can be attributed to the increased optical path length and improved impedance matching at longer wavelengths, which strengthen light–matter interaction within the dielectric layer. On the basis of this observation, four thicknesses (h2 = 105, 115, 125, and 135 nm) exhibiting relatively high absorptivity beyond 3000 nm were selected for further comparison, as illustrated in Fig. 2(b). From the enlarged spectral view, it is evident that all four thicknesses exhibit a slight reduction in absorptivity near a wavelength of approximately 300 nm. This decrease is primarily associated with impedance mismatch and reduced dielectric loss in the UV region. Among the four candidates, the h2 layer thickness of 115 nm exhibits the smallest absorptivity degradation in the UV range while maintaining strong absorption at longer wavelengths. Consequently, h2 = 115 nm was selected as the optimal thickness, offering a balanced absorption performance across the UV-to-MIR spectral range.

Figure 3(a) presents the parametric thickness sweep of the h3 Cr layer, performed over a range of 5 to 30 nm with a step size of 5 nm. As indicated in the left panel, the configuration with h3 = 5 nm and 10 nm exhibits a pronounced reduction in absorptivity at wavelengths beyond approximately 1500 nm compared with the other cases. This degradation is attributed to insufficient metallic loss and weak plasmonic coupling at longer wavelengths when the Cr layer is very thin. Consequently, these two thicknesses were excluded from further consideration. In contrast, for thicker Cr layers (h3 = 25 and 30 nm), the absorptivity decreases notably in the wavelength range of 1000–1250 nm and again beyond 2500 nm. This behavior suggests that excessive metallic thickness leads to increased reflectivity and impedance mismatch, thereby suppressing broadband absorption. After excluding these suboptimal cases, only h3 = 15 and 20 nm were retained for detailed comparison. As shown in the remaining spectra, the h3 = 20 nm configuration demonstrates slightly superior overall absorptivity across a broad wavelength

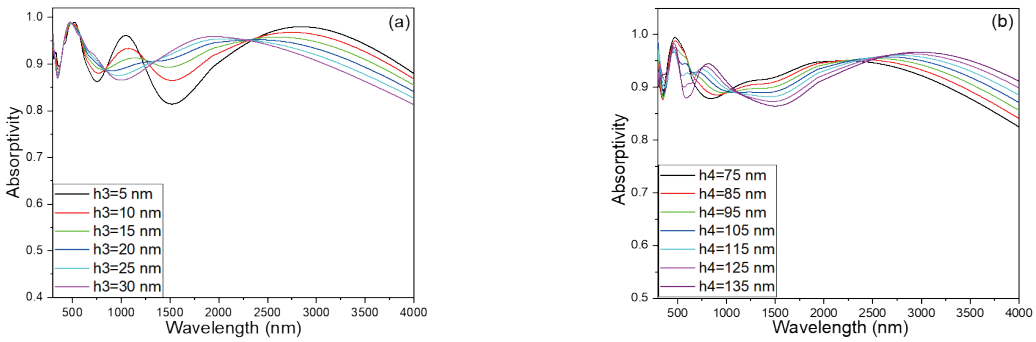

Fig. 3. (Color online) Effects of thickness variations of (a) h3 Cr and (b) the h4 Si_3N_4 layers on absorption spectra.

range from approximately 750 to 2500 nm compared with h3 = 15 nm. This improvement indicates a more favorable balance between intrinsic material loss and impedance matching. Therefore, the thickness of 20 nm was selected as the optimal parameter for the h3 layer.

Figure 3(b) illustrates the parametric thickness sweep of the h4 Si_3N_4 layer, conducted over a range of 75 to 135 nm with a step size of 10 nm. As observed in Fig. 3(b), within the wavelength interval from 300 to 1000 nm, only the configuration with h4 = 115 nm maintains absorptivity consistently above 0.900 across the entire spectral range. Under this condition, the absorption bandwidth can extend from 300 to 3850 nm, and the average absorptivity within this spectral range reaches 0.928. For thinner or thicker Si_3N_4 layers, notable absorption degradation appears in portions of the UV and visible regions, indicating suboptimal impedance matching and insufficient optical confinement. The superior performance when h4 = 115 nm can be attributed to the optimized dielectric thickness, which effectively balances multiple interference conditions and enhances light trapping within the multilayer structure. This optimized thickness promotes constructive absorption across short and intermediate wavelengths while avoiding excessive reflection caused by impedance mismatch. As a result, h4 = 115 nm provides the most uniform and robust absorption behavior in the UV–visible spectral region. Therefore, this thickness was selected as the optimal parameter for the h4 layer in the subsequent design optimization.

Compared with the multilayer structure reported in Ref. 13, which employs SiO_2 and Cr as the constituent materials and achieves an average absorptivity of 0.964 over a bandwidth of 380–2138 nm, the absorber proposed in this study utilizes Si_3N_4 and Cr and exhibits a slightly lower average absorptivity of 0.928 over a significantly broader wavelength range of 300–3850 nm. Although the average absorptivity is marginally reduced, replacing SiO_2 with Si_3N_4 markedly enhances absorption in the IR region, particularly within the wavelength range of approximately 1400–3500 nm. This improvement can be attributed to the higher refractive index and stronger optical confinement provided by Si_3N_4, which promote enhanced light–matter interaction and more effective impedance matching at longer wavelengths. As a result, the absorption spectrum is substantially extended into the MIR region, leading to a pronounced expansion of the overall operational bandwidth. These findings demonstrate that substituting SiO_2 with Si_3N_4 represents an effective strategy for achieving ultra-broadband absorption, especially when wide spectral coverage is prioritized over maximizing average absorptivity within a narrower band.

The comparison with the Cr–SiO_2 absorber reported by Hsu *et al.*[12] further indicates that the improvement originates primarily from the intrinsic optical properties of the dielectric material rather than from a substantial change in structural complexity. Owing to the higher refractive index of Si_3N_4, stronger electromagnetic field confinement is achieved inside the multilayer stack, resulting in improved impedance matching and more efficient light trapping at longer wavelengths. Consequently, the proposed absorber extends the high-absorption region from the UV–NIR range reported for the Cr–SiO_2 structure into the MIR while preserving the same simple two-material multilayer concept. These results suggest that replacing SiO_2 with Si_3N_4 provides an effective material strategy for extending the operational bandwidth without introducing additional materials or more complex nanostructures. Table 1 shows a comparison of the previously reported Cr–SiO_2 absorber with the proposed Si_3N_4/Cr absorber. Both designs

Table 1
Characteristics of the reported Cr–SiO_2 and proposed Si_3N_4/Cr absorbers.

Item	Ref. 12 (Hsu *et al*., 2025) Cr–SiO_2 absorber	This work Si_3N_4/Cr absorber
Constituent materials	Cr + SiO_2	Cr + Si_3N_4
Number of materials	2	2
Optimization method	Layer-by-layer thickness optimization	Layer-by-layer thickness optimization
Top resonator	Cr cylinder	Cr cylinder
High-absorption range (A > 0.900)	200–2160 nm	300–3850 nm
Bandwidth	1960 nm	3550 nm
Average absorptivity	0.950	0.928
Spectral coverage	UV–NIR	UV–visible–MIR
Main advantage	Higher average absorptivity	Much broader operating bandwidth
Dielectric property	Lower refractive index (SiO_2)	Higher refractive index (Si_3N_4)
IR performance	Limited beyond ~2160 nm	Extended to ~3850 nm
Structural complexity	Simple planar multilayer	Simple planar multilayer
Potential applications	Solar absorber, optical absorption	Broadband optical sensing, photodetection, photothermal devices

adopt the same two-material multilayer concept and a similar layer-by-layer optimization procedure. Although the proposed absorber exhibits a slightly lower average absorptivity, replacing SiO_2 with Si_3N_4 substantially extends the high-absorption bandwidth from 200–2160 nm to 300–3850 nm, demonstrating the advantage of the higher-refractive-index dielectric for broadband IR absorption.

Compared with representative ultra-broadband absorbers reported in recent studies, the proposed Si_3N_4/Cr absorber provides a competitive balance between bandwidth, structural simplicity, and fabrication feasibility. Many previously reported absorbers achieve high average absorptivity by employing three or more constituent materials, metasurfaces, nanocone arrays, or multilayer hybrid nanostructures. In contrast, the present design employs only two materials and a predominantly planar multilayer architecture with a single cylindrical resonator, while maintaining absorptivity higher than 0.900 over a continuous wavelength range of 300–3850 nm. Therefore, although the average absorptivity is slightly lower than that of several reported absorbers, the proposed design offers a considerably broader operating bandwidth together with a significantly reduced fabrication complexity, making it attractive for practical broadband optical sensing and photonic applications.

Note that the deposition of Si_3N_4 films can be realized using several mature thin-film techniques. Although high-quality stoichiometric Si_3N_4 is frequently deposited by low-pressure chemical vapor deposition at elevated temperatures, low-temperature plasma-enhanced chemical vapor deposition (PECVD) and reactive magnetron sputtering are also widely adopted for multilayer photonic devices. These deposition techniques substantially reduce the thermal budget and improve compatibility with underlying Cr thin films. Consequently, the proposed Si_3N_4/Cr multilayer architecture remains compatible with existing thin-film fabrication technologies while preserving the advantages of using only two constituent materials. In future

experimental studies, we will investigate the optimization of deposition conditions and interface quality to further validate the proposed design.

From a practical fabrication viewpoint, the proposed structure is compatible with mature thin-film fabrication technologies. The Si_3N_4 dielectric layers can be deposited by PECVD or sputtering, while the Cr layers can be prepared by magnetron sputtering or electron-beam evaporation. Because the absorber employs only two constituent materials and a predominantly planar multilayer architecture, repeated material switching and complex lithographic processing are minimized, thereby improving deposition compatibility and manufacturing reproducibility. In practical fabrication, slight variations in film thickness and surface roughness are unavoidable. However, because the broadband absorption of the proposed structure originates from the collective coupling of multiple dielectric–metal interfaces rather than from a single high-Q resonance, moderate fabrication imperfections are expected to have only a limited effect on the overall absorption bandwidth. This structural tolerance further enhances the feasibility of realizing the proposed absorber using current thin-film manufacturing technologies.

From a quantitative perspective, the proposed Si_3N_4/Cr absorber increases the high-absorption bandwidth (absorptivity > 0.900) from 1960 to 3550 nm, corresponding to an approximately 81% increase compared with the previously reported Cr–SiO_2 absorber. Although the average absorptivity decreases slightly from 0.950 to 0.928 (approximately 2.3%), the operating spectral range is substantially extended from the UV–NIR region to the UV–visible–MIR region. Furthermore, the impedance analysis presented in Fig. 5 shows that the normalized impedance remains close to unity over almost the entire operating wavelength range, confirming that the improved IR absorption originates from enhanced impedance matching rather than increased material loss alone. Since both absorbers employ the same planar multilayer architecture and identical optimization methodology, the observed performance enhancement can be directly attributed to the substitution of SiO_2 with Si_3N_4.

Subsequently, the thickness parameters of the remaining layers were further examined to evaluate their effect on the absorption performance. The results reveal that the originally selected parameters already correspond to the optimal design configuration. In particular, the thicknesses of the h5, h6, h7, h8, and h9 layers, as well as the cylinder diameter D, jointly contribute to achieving stable and efficient ultra-broadband absorption; therefore, no further optimization is required. As a representative example, Fig. 4(a) illustrates the effects of thickness variations of the h6 Si_3N_4 layer on the absorption spectra. When the thickness of the h6 layer is reduced to 75 nm, the effective absorption bandwidth shrinks to 300–3500 nm, accompanied by a slight decrease in average absorptivity to 0.922. This behavior indicates reduced optical confinement and weaker impedance matching, particularly at longer wavelengths. In contrast, when the thickness of the h6 layer is increased to 95 nm, a distinct absorption valley with absorptivity falling below 0.900 emerges in the wavelength range of approximately 580–680 nm.

As the h6 layer thickness is further increased, this absorption dip becomes broader and more pronounced, suggesting the onset of destructive interference and increased reflection losses that disrupt broadband absorption continuity. These observations confirm that the originally designed thickness of 85 nm provides the most favorable balance between optical path enhancement and impedance matching, thereby yielding optimal broadband absorption

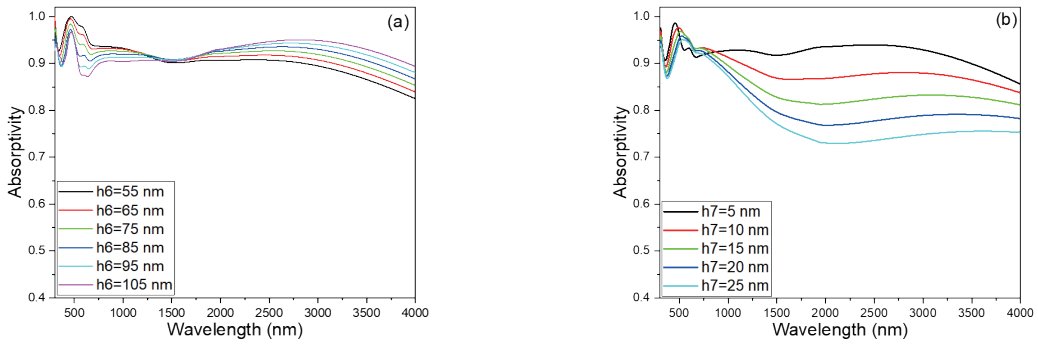

Fig. 4. (Color online) Effects of thickness variations of (a) h6 Si_3N_4 and (b) h7 Cr layers on absorption spectra.

performance. A similar trend is observed for the h7 Cr layer, as shown in Fig. 4(b). When the thickness of the h7 layer is increased to 10 nm, the absorptivity in the IR region begins to decline, with portions of the spectrum dropping below 0.900. Further increases in h7 layer thickness lead to a more severe degradation of IR absorption, primarily owing to excessive metallic loss and enhanced reflectivity, which hinder efficient light penetration into the underlying dielectric layers. Consequently, the originally selected thickness of 5 nm for the h7 layer is identified as the optimal value. On the basis of the results of these comprehensive analyses, the h5, h6, h7, h8, and h9 layer thicknesses, and D are retained at their original design values and are not further discussed in the subsequent sections. Table 2 shows the differences in these parameters between their initial design (I) and optimized (O) values.

Optical impedance analysis provides valuable insight into the reflection and absorption behavior of electromagnetic waves within the absorber, and it can be characterized by its real and imaginary components. Note that the impedance values presented in Fig. 5 are normalized with respect to the free-space impedance. Under this normalization, a real part approaching unity and an imaginary part approaching zero indicate excellent impedance matching between the absorber and the free space, thereby minimizing reflection. Since the bottom Cr reflector effectively suppresses optical transmission, the absorption characteristics are governed primarily by the reflection coefficient, which is consistent with the relation $A \approx 1-R$. When the real part of the normalized impedance approaches unity, it indicates good impedance matching between the material and the free space, allowing incident electromagnetic energy to enter the structure efficiently with minimal reflection. An imaginary part close to zero signifies low reactive energy storage and minimal loss due to impedance mismatch. The impedance profile shown in Fig. 5 further demonstrates that the normalized impedance remains close to unity throughout most of the operating wavelength range, indicating that the extended IR absorption is achieved while preserving effective impedance matching. As shown in Fig. 5, the real part of the

Table 2
Initial design parameters (*I*) and optimized geometric parameters (*O*). Unit: nm.

	h1	h2	h3	h4	h5	h6	h7	h8	h9	D
I	100	85	6	85	6	85	6	20	100	165
O	100	115	20	115	6	85	5	20	100	165

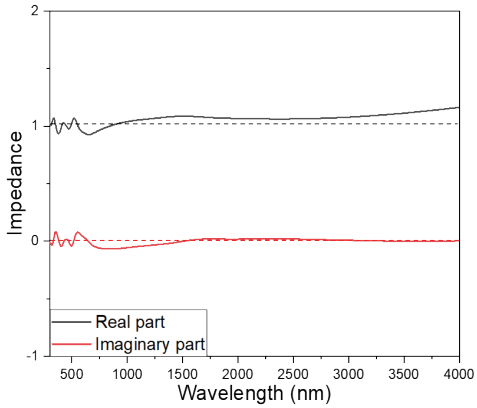

Fig. 5. (Color online) Optical impedance of the proposed structure as a function of wavelength under optimized parameters.

impedance remains slightly higher than 1 over the wavelength range from 300 to 3800 nm, yet remains stays very close to unity throughout this region. This near-ideal impedance matching explains the high absorptivity achieved across the UV, visible, and IR bands. However, when the wavelength exceeds approximately 3800 nm, the real part of the impedance gradually deviates from 1, indicating deteriorated impedance matching. As a result, incident electromagnetic waves are no longer efficiently coupled into the absorber, which accounts for the observed limitation of the effective absorption bandwidth to around 3800 nm. In contrast, the imaginary part of the impedance remains close to zero over a broad wavelength range from 300 to 4000 nm, implying minimal reactive loss and weak energy storage effects. This behavior confirms that the absorber primarily dissipates energy through intrinsic material loss mechanisms rather than reflective or reactive processes. Overall, the impedance analysis corroborates that the ultra-broadband absorption performance of the proposed structure originates from effective impedance matching over a wide spectral range, which plays a decisive role in achieving high absorptivity. Therefore, the impedance analysis, together with the negligible optical transmission enabled by the optically thick Cr reflector, provides a consistent physical explanation for the observed ultra-broadband absorption behavior.

In the results shown in Fig. 4(b) for h7 = 5 nm, the optimized absorption spectrum exhibits pronounced absorption peaks at wavelengths of approximately 450, 600, 760, and 2860 nm.

Therefore, the electric and magnetic field distributions at these representative wavelengths were analyzed, and the corresponding results are presented in Figs. 6(a) and 6(b). As observed in Fig. 6, clear resonant phenomena are evident at the absorption peaks, indicating strong electromagnetic field enhancement within the absorber structure at these wavelengths. From the electric field distributions, it can be observed that for all absorption peaks, strong localized electric field intensification occurs around the top-layer cylindrical structures. This behavior indicates the excitation of localized surface plasmons (LSPs), which arise from the strong interaction between incident electromagnetic waves and the metallic nanostructures. Moreover, as the absorption peak shifts toward longer wavelengths, the contribution of the Cr substrate becomes more pronounced, as evidenced by the reduction in the number of low-field (blue) regions.

This observation suggests improved energy confinement and absorption efficiency in the long-wavelength regime, facilitated by enhanced coupling between the top resonator and the underlying metallic layers. In addition, the magnetic field distributions reveal the presence of strongly confined magnetic fields propagating along the metal–dielectric interfaces. This feature is characteristic of propagating surface plasmons (PSPs), which play a crucial role in extending the absorption bandwidth by enabling efficient energy transport and dissipation along the multilayer interfaces. The coexistence of LSP and PSP resonances confirms that the ultra-broadband absorption performance of the proposed absorber originates from the synergistic coupling of localized and propagating plasmonic modes across different wavelength regimes. The field distributions also provide indirect evidence of the coupling mechanism. At shorter wavelengths (450–760 nm), the electric field is predominantly concentrated around the top Cr cylindrical resonator, indicating that LSP excitation is the dominant absorption mechanism. As the wavelength increases to the MIR region (2860 nm), the electromagnetic field extends further along the metal–dielectric interfaces and penetrates deeper into the multilayer stack, indicating an increasing contribution from PSP modes. This wavelength-dependent evolution of the field

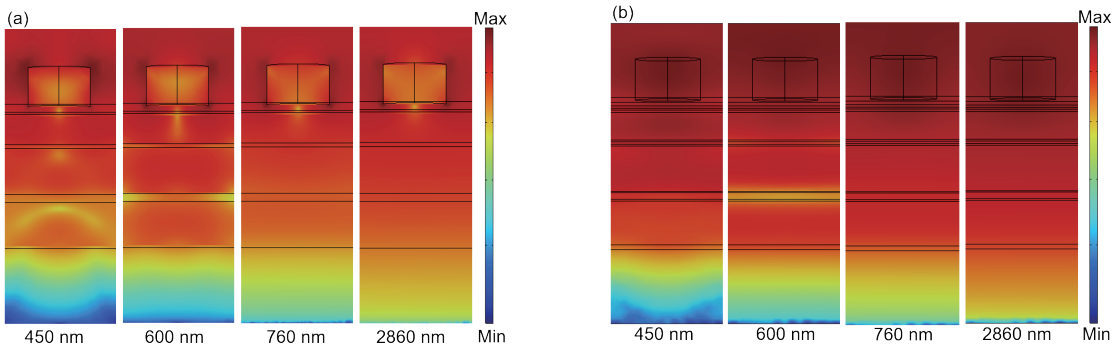

Fig. 6. (Color online) Simulated (a) electric and (b) magnetic field intensity distributions of the proposed ultra-broadband absorber under normal incidence of TE-polarized waves at selected wavelengths.

distribution is consistent with the impedance profile shown in Fig. 5, where the normalized impedance remains close to unity throughout most of the operating spectral range. The simultaneous observation of localized field enhancement, interface-guided energy confinement, and near-unity impedance matching provides mutually consistent evidence supporting the proposed plasmonic coupling mechanism responsible for the ultra-broadband absorption. These impedance characteristics are also consistent with the field distributions presented in Fig. 6, indicating that efficient impedance matching facilitates the excitation and coupling of both localized and propagating plasmonic modes over a broad wavelength range. Although the present study is based on numerical simulations, the proposed absorber has been intentionally designed using materials and geometries that are compatible with existing microfabrication technologies, providing a realistic pathway toward future experimental implementation.

From an application perspective, the ultra-broadband operating range of 300–3850 nm enables the proposed absorber to support multiple photonic and sensing functions across different spectral regions. The UV region (300–400 nm) is particularly suitable for UV photodetectors and environmental monitoring systems, where high absorptivity can improve photon utilization and enhance detector responsivity. The visible region (400–700 nm) is advantageous for broadband optical sensing and imaging applications because efficient light harvesting contributes to stable optical signals and improved signal-to-noise performance. The NIR region (700–2500 nm) is well suited for optical communication monitoring, biomedical sensing, and multispectral photodetection, while the extended MIR region (2500–3850 nm) is especially attractive for thermal sensing, photothermal conversion, IR imaging, and molecular spectroscopy, where many characteristic vibrational absorption bands are located. Because the proposed absorber maintains absorptivity above 0.900 throughout this wide spectral range together with near-unity impedance matching, incident electromagnetic energy can be coupled efficiently into the absorber with minimal reflection loss. Consequently, the proposed design is expected to improve practical device metrics, including optical energy utilization, detector responsivity, photothermal conversion efficiency, and operational stability under broadband illumination. These characteristics make the proposed absorber a promising platform for multifunctional photonic and sensing devices.

4. Conclusions

In this study, an ultra-broadband optical absorber operating from the UV to the MIR region was successfully designed and analyzed using a simplified material system consisting solely of Si_3N_4 and Cr. By adopting a predominantly planar multilayer architecture with a Cr cylindrical top layer, the proposed nine-layer structure achieves absorptivity exceeding 0.900 over an exceptionally wide wavelength range of 300–3850 nm, with an average absorptivity of approximately 0.928. Systematic parametric optimization confirmed that the initially selected geometric parameters represent near-optimal values, as deviations in layer thicknesses led to bandwidth narrowing or the emergence of absorption valleys owing to impedance mismatch and weakened resonance coupling. Electromagnetic field analyses revealed that the broadband absorption originates from the synergistic contribution of LSP resonances excited around the Cr

cylinders and the PSP modes at the metal–dielectric interfaces, together with effective interference and light-trapping effects within the multilayer stack. Optical impedance analysis further demonstrated excellent impedance matching to free space across most of the operational bandwidth, explaining the high absorption efficiency. Compared with previous SiO_2/Cr-based designs, replacing SiO_2 with Si_3N_4 effectively enhances IR absorption and significantly extends the operational bandwidth, albeit with a modest reduction in average absorptivity. Overall, this work demonstrates that high-performance ultra-broadband absorbers can be realized using only two low-cost materials and a fabrication-friendly planar design, offering strong potential for practical applications in sensing, photothermal energy conversion, and optoelectronic devices. Moreover, owing to its simple two-material multilayer configuration and compatibility with conventional thin-film deposition techniques, the proposed absorber provides a practical platform for future experimental fabrication and validation, facilitating its application in broadband optical sensing, photothermal devices, and integrated photonic systems.

Acknowledgments

This work is supported by Summit-Tech Resource Corp. and by projects under grant nos. NSTC 113-2221-E-390-011 and NSTC 114-2622-E-390-001. We would be like to thank the staff of Pitotech Co., Ltd., for instructing us on the use of COMSOL Multiphysics® software.

References

1 A.E. Assal, H. Breiss, R. Benzerga, and A. Sharaiha: J. Mater. Sci. **56** (2021) 19484.
2 M. Avraham and Y. Nemirovsky: Sensors **25** (2025) 6819.
3 A. Sharma, J. Kedia, and N. Gupta: Opt. Eng. **60** (2021) 090901.
4 Y. Zhang, K. Ebata, M. Iimori, Q. Liu, Z. Zhao, R. Takeuchi, H. Li, K. Maenaka, and K. Hirakawa: Microsyst. Nanoeng. **11** (2025) 132.
5 N. S. Shrikrishna, R. Sharma, J. Sahoo, A. Kaushik, and S. Gandhi: Chem. Eng. J. **490** (2024) 151661.
6 B. Kaur, S. Kumar, J. Nedoma, R. Martinek, and C. Marques: APL Photonics **9** (2024) 091102.
7 B. X. Wang, C. Xu, G. Duan, W. Xu, and F. Pi: Adv. Funct. Mater. **33** (2023) 2213818.
8 P. P. Nakti, D. Sarker, M. I. Tahmid, and A. Zubair: Nanoscale Adv. **5** (2023) 6858.
9 F. Yang, R. H. Li, S. L. Tan, J. W. Dong, and S. J. Jiang: Nanophotonics **12** (2023) 2451.
10 W. Chen, J. Liu, W. Ma, G. X. Yu, J. Q. Chen, H. Cai, and C. F. Yang: Appl. Sci. **10** (2020) 3276.
11 G. Peng, P. X. Ke, L. C. Tseng, C. F. Yang, and H. C. Chen: Photonics **10** (2023) 804.
12 W. L. Hsu, X. Y. Lin, C. M. Ho, C. F. Yang, and K. K. Lai: Photonics **12** (2025) 907.
13 T. Sang, H. Qi, X. Wang, X. Yin, G. Li, X. Niu, B. Ma, and H. Jiao: Nanomaterials **10** (2020) 1625.